Variability and forcing of the East Australian Current

Melissa M. Bowen[1]
Colorado Center for Astrodynamics Research, University of Colorado, Boulder, Colorado, USA

John L. Wilkin
Institute of Marine and Coastal Sciences, Rutgers University, New Brunswick, New Jersey, USA

William J. Emery
Colorado Center for Astrodynamics Research, University of Colorado, Boulder, Colorado, USA

Received 17 June 2004; revised 1 December 2004; accepted 26 January 2005; published 23 March 2005.

[1] The spatial and temporal variability of the East Australian Current (EAC) is investigated using 6 years (1993–1998) of surface geostrophic stream function from an optimal interpolation of altimeter sea surface heights and velocities derived from tracking thermal features in satellite imagery. Variability appears as a series of cyclones and anticyclones propagating southwestward and westward with periods between 90 and 180 days. The behavior of the variability changes over the 6 years. Energy in the mesoscale frequencies moves slowly south and diminishes with more westward propagation in the region where the current separates from the coast. We find no evidence for a consistent forcing of the EAC by mesoscale signals propagating westward from the South Pacific basin. We suggest that the observations are consistent with variability originating between 32°S and 35°S through intrinsic instabilities of the current.

Citation: Bowen, M. M., J. L. Wilkin, and W. J. Emery (2005), Variability and forcing of the East Australian Current, *J. Geophys. Res.*, *110*, C03019, doi:10.1029/2004JC002533.

1. Introduction

[2] The East Australian Current (EAC) flows poleward along the eastern Australian coast (Figure 1). Along with the poleward-flowing currents along the eastern coast of New Zealand, the EAC forms the western boundary current system of the South Pacific subtropical gyre. Transport in the main stream of the EAC along the Australian Coast, between about 17°S and 32°S, has been estimated to be between 22 and 30 Sv [*Mata et al.*, 2000; *Ridgway and Dunn*, 2003], in agreement with the transport predicted by a Sverdrup balance with the gyre-scale winds [*Mata et al.*, 2000]. At about 32°S the current often turns sharply offshore to flow southeastward into the Tasman Sea. The persistence of this behavior has been attributed to coastline curvature [*Godfrey et al.*, 1980], the structure of the gyre-scale wind stress curl [*Tilburg et al.*, 2001], and the blocking of westward propagating Rossby waves by New Zealand [*Nilsson and Cresswell*, 1981].

[3] At times the EAC can extend along the coast well south of the main separation region. During these times it breaks into a number of eddies, some of which escape into the Tasman Sea, others of which move northeastward to coalesce with the main current [*Nilsson and Cresswell*, 1981]. A number of studies have found a strong periodicity between 90 and 140 days in the separation region. *Boland* [1979] discerned a 90 day signal from repeat XBT lines at 35°S and a suggestion of westward propagation of the eddies. *Walker and Wilkin* [1998] note periodicity near 100 days in satellite sea surface temperatures over the region. Sea surface height anomalies from satellite altimetry reveal a 130 day periodicity [*Feron*, 1995]. Two years of current meter records from the WOCE PCM-3 array at 30°S show the variations are dominated by 90 to 140 day periods, often accompanied by a reversal of the flow to the north over the entire water column [*Mata et al.*, 2000]. *Mata et al.* [2000] use sea surface temperatures from satellites to link these reversals to a movement of the current away from the coast in an eddy shedding process.

[4] The control of the eddy shedding has been attributed to several different mechanisms. *Stammer* [1997] notes that compared to other regions the EAC has an anomalously weak correspondence between eddy kinetic energy, inferred from altimeter measurements of sea surface height, and kinetic energy of the mean flow derived from climatology. On the basis of this and the large length scales in the current he suggests eddy activity in the EAC could be more barotropic in nature rather than generated by baroclinic instability. *Nilsson and Cresswell* [1981] suggest that the creation of eddies south of the separation region is the result of oscillations in the Tasman Front propagating westward and "breaking" against the coast. *Marchesiello and Middleton* [2000] also infer that this process is responsible for eddy shedding in model simu-

[1]Now at National Institute of Water and Atmospheric Research, Wellington, New Zealand.

0148-0227/05/2004JC002533$09.00

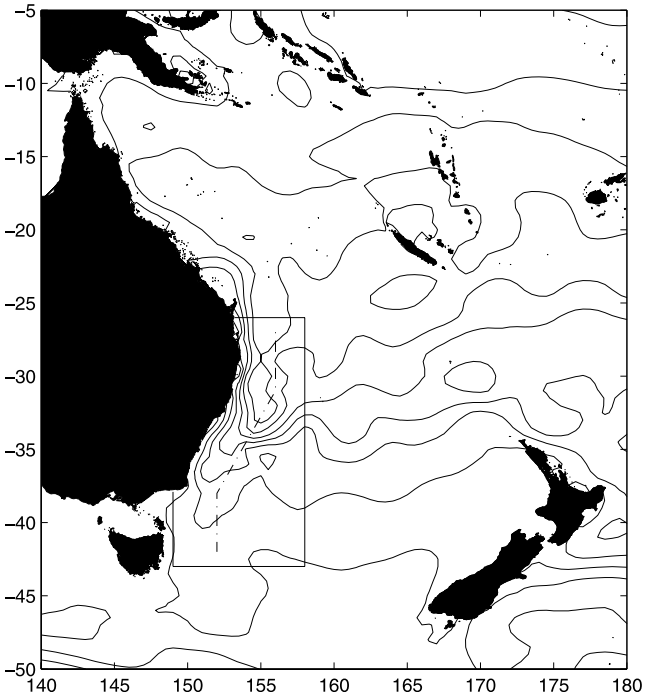

Figure 1. Study region (solid lines) enclosing the main flow of the East Australian Current, evident in the surface dynamic height relative to 2000 m from the Commonwealth Scientific and Industrial Research Organisation (CSIRO) Atlas of Regional Seas (CARS) climatology [*Ridgway and Dunn*, 2003] (10 cm contour intervals). The dash-dotted line 250 km from the coast is used to display later analyses.

lations focused on the separation region. *Cresswell and Legeckis* [1986] suggest a quite different source of mesoscale activity: using satellite thermal imagery and drifter observations they observe that eddy formation and absorption may involve "geopotential ridges" arriving from the north.

[5] Studies of variability in the Kuroshio and Agulhas currents have suggested fluctuations with periods near 100 days may propagate from regions of high eddy kinetic energy in the adjacent ocean basins and modulate the currents [*Zhang et al.*, 2001; *Schouten et al.*, 2002]. A similar band of eddy kinetic energy is situated in the western Pacific between 20°S and 30°S, corresponding to a region of enhanced density gradients in climatologies [*Stammer*, 1997; *Qiu and Chen*, 2004]. The band of higher variance lies near the zero in the wind stress curl, which defines the northern edge of the subtropical gyre and convergence of meridional Sverdrup transport into zonal flows [*Trenberth et al.*, 1990]. The region appears to stretch to the edge of the EAC and could be influential in its behavior.

[6] Despite overwhelming evidence that considerable variance in the EAC lies at mesoscale frequencies (90–180 days), there has been little description of the spatial nature of the variability. In addition a number of different mechanisms have been put forward for how the variability is being forced. Here we analyze 6 years of surface currents in the region to describe this variability and investigate further the possibility that mesoscale fluctuations of sea surface height in the Pacific gyre to the northeast of the EAC may be responsible for variations in the current.

2. Methods

2.1. Observations

2.1.1. Surface Stream Function in the East Australian Current

[7] Surface stream function and velocities were derived from two types of satellite observations, velocities extracted from tracking thermal features in sequential thermal imagery using the maximum cross correlation (MCC) technique and sea surface height anomalies derived from satellite altimetry. The two independent sets of measurements were then merged using an optimal interpolation onto a stream function on a regular grid in both space and time.

[8] The velocities derived from the thermal imagery are described in detail elsewhere [*Bowen et al.*, 2002] and only summarized briefly here. The velocities were obtained several times daily by tracking features in sequential thermal images using the MCC technique [*Schmetz and Nuret*, 1987; *Emery et al.*, 1986; *Kelly and Strub*, 1992] applied to 6 years of high-resolution imagery. Before combining with the sea surface heights from the altimetry, the MCC velocities were composited in 3 day segments that lower the apparent noise variance of the velocities, minimize ageostrophic motions in the velocities, and reduce the amount of data to a manageable level. The 6 year mean of the velocities was removed to create a velocity anomaly before combining with the sea level anomalies.

[9] Altimeter sea level anomalies (SLAs) over the same region were obtained from all available Archiving, Validation, and Interpretation of Satellite Oceanographic Data (AVISO) SLAs consisting of data from the TOPEX/Poseidon, ERS-1, and ERS-2 altimeters. The standard corrections were applied to the data (ionosphere, wet and dry troposphere, sea state bias, CSR ocean and loading tides, pole tide, solid earth tide, inverse barometer) as described more fully by *AVISO* [1998]. The mean at each location was removed and sea levels were filtered along track with a 10-point boxcar filter to reduce noise and retain the geostrophic signal.

[10] As described in detail by *Wilkin et al.* [2002], the thermally derived velocities and altimetric height estimates were mapped to a gridded geostrophic stream function using an optimal interpolation. The covariance functions used in the interpolation were derived from the observations: a spatial covariance function of the form of *Le Traon and Hernandez* [1992] with length parameter of 65 km (corresponding to a zero crossing of about 200 km) and an exponential temporal covariance function with timescale of 10 days were used.

[11] To illustrate the data sets, Figure 2 shows the MCC velocities averaged over 3 days around 30 September 1998, from which the 6 year mean velocities have been removed. An optimal interpolation based only on the altimeter sea surface heights captures many of the same features seen in the MCC currents. An optimal interpolation including both the sea surface heights and the MCC currents changes the position and strength of some of the features.

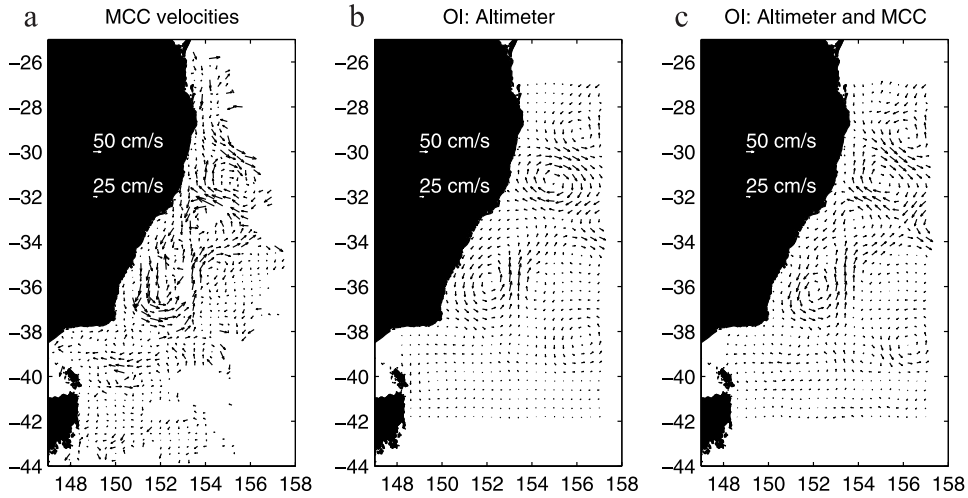

Figure 2. Surface current anomalies from (a) maximum cross correlation (MCC) velocities between 29 September and 1 October 1998, (b) an optimal interpolation of altimeter sea surface heights to a geostrophic stream function for 30 September 1998, and (c) an optimal interpolation including both altimeter sea surface heights and the MCC velocities.

2.1.2. Sea Surface Height Anomalies in the Pacific Basin

[12] The observed variability in the EAC region was linked to open ocean variability in the South Pacific basin using the sea surface height anomaly mapped product (MSLAs) from AVISO. The maps used are a merged data product created from sea level anomalies measured by TOPEX/Poseidon, ERS-1, and ERS-2 altimeters [*Ducet et al.*, 2000].

2.2. Analysis

[13] Variance ellipses were calculated from the 6 year time series at each independent location to show the strength and direction of the variability. The eddy momentum fluxes from the velocity anomalies were also used to estimate the conversion of eddy kinetic energy to mean kinetic energy. As shown elsewhere [*Qiu*, 1995; *Wilkin and Morrow*, 1994; *Brooks and Niiler*, 1977], the baroclinic conversion terms in the mean kinetic energy balance are

$$\overline{u'u'}\frac{\partial \overline{u}}{\partial x} + \overline{u'v'}\frac{\partial \overline{u}}{\partial y} + \overline{v'u'}\frac{\partial \overline{v}}{\partial x} + \overline{v'v'}\frac{\partial \overline{v}}{\partial y}, \qquad (1)$$

where overbars indicated long-term time averaged quantities and primes indicate time fluctuations. When the sum is positive (negative), the mean flow gains (loses) energy from (to) the eddies. The gradients in the mean flow were derived from the Commonwealth Scientific and Industrial Research Organisation (CSIRO) Atlas of Regional Seas (CARS) climatology [*Ridgway and Dunn*, 2003] assuming a level of no motion at 2000 m. Another mean flow from the 6 years of MCC velocities produced similar results but has less spatial coverage than the CARS climatology.

[14] Spectra of the stream function, zonal and meridional velocities were calculated for the entire region by averaging together the spectra taken over the entire windowed time series at each location.

[15] Frequency domain empirical orthogonal functions (EOFs) were used to characterize the propagating features in the region following the method of *Barnett* [1983]. The EOFs were derived by first filtering the data to isolate the mesoscale frequencies (corresponding to periods between 90 and 180 days), then forming an analytic signal at each location with the Hilbert transform to capture phase information about the signal. The analysis provides spatial maps of amplitude and phase for each mode as well as the time evolution of amplitude and phase of each mode.

[16] Frequency content was separated in space and time using a wavelet analysis following the method of *Torrence and Compo* [1998]. A complex Morlet wavelet (Figure 3), a plane wave modulated by a Gaussian envelope, was chosen as a basis function to capture the slowly varying, ubiquitous oscillations in the region. Unlike a Fourier transform, which produces one measurement of frequency content for the entire time series, the wavelet function windows the time series evaluating the evolution of the variance at each frequency. The wavelets capture the evolution of the amplitude of a wave packet, corresponding to the definition of group velocity and energy flow; in contrast, analyses such as Hovmöller diagrams and Radon transforms find linear features in the observations, corresponding to phase velocity. *Meyers et al.* [1993] show an example of a Yanai wave

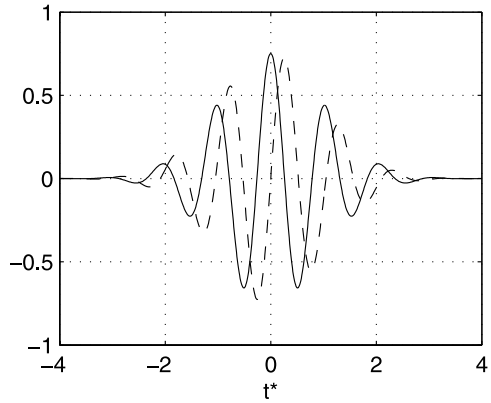

Figure 3. Real (solid line) and imaginary (dashed line) parts of the Morlet wavelet base.

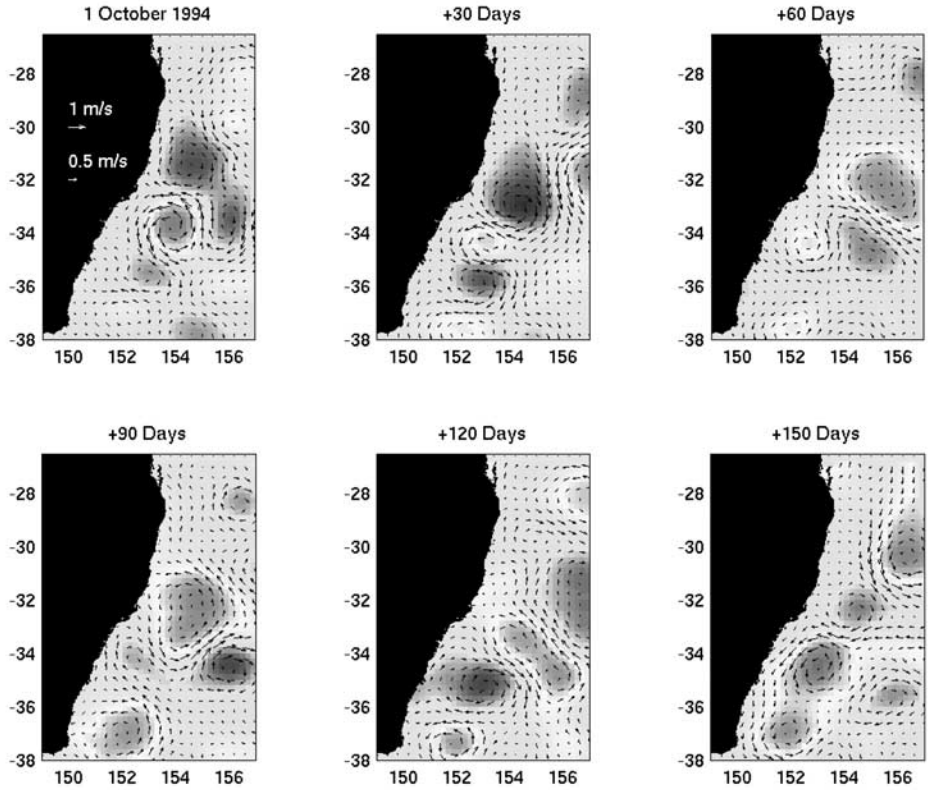

Figure 4. Snapshots of stream function anomaly and associated geostrophic current anomaly over a 150 day period showing alternating cyclones and anticyclones. See color version of this figure at back of this issue.

in which phase velocity is westward but a wavelet transform captures the group velocity of the eastward moving energy.

[17] The wavelet analysis was applied to the time series at each location and the wavelet power spectra over the mesoscale frequencies averaged together. A significance level was determined (in a manner similar to determining significance of peaks in a Fourier series) by comparing to the spectrum of a Markov process with autocorrelation and variance of the observations. Red contours have been added on top of the power spectrum contours to show regions where the wavelet power is significantly different at the 95% level from the red noise spectrum at that location.

[18] To trace mesoscale frequencies coming into or out of the region an identical wavelet analysis was also performed on time series of the AVISO gridded sea surface heights in a region of the southwest Pacific adjacent to the current.

3. Results

3.1. Variability in the East Australian Current

[19] Animating the 6 years of stream function shows ridges and troughs appearing in turn at the northern extreme of the region and moving southwestward before breaking into more distinct eddies at the separation point near 32°S (Figure 4). Much of the time, a train of alternating cyclonic and anticyclonic anomalies continue along the coast south of 32°S, occasionally appearing to rotate around one another in an anticyclonic direction, moving anomalies into the Tasman Sea and interacting with the disturbances coming from the north.

[20] The passage of the cyclones and anticyclones along the coast can be seen in the variance ellipses calculated from the geostrophic velocities (Figure 5a). Ellipses are oriented parallel to the coast in the region nearest it, turning perpendicular to the coast farther offshore, and then back to parallel farther from the coast. The region of highest eddy kinetic energy is not associated with the strongest mean current, which is in the northern part of the region, but with the area just south of where the mean current separates from the coast (Figure 5b).

[21] The barotropic conversion terms in the mean kinetic energy balance (Figure 6) show a number of areas with negative values that suggest regions where the mean flow loses energy to the eddies. The greatest negative values, located where the main current separates from the coast, indicate this area is likely to be a source of barotropic eddy energy.

[22] The spectrum of the stream function shows three distinct peaks, centered at approximately annual, 165, and 115 day periods, each peak containing about 15% of the total variance in the entire region (Figure 7). Spectra of geostrophic velocities derived from the stream function also have peaks at the two higher frequencies but little signal at the annual frequency. The meridional velocity has more energy at 115 days than at 165 days, implying more zonal structure in the stream function at the higher frequency. A small peak near 60 days in the spectra is aliasing of the semidiurnal tides in the TOPEX/Poseiden altimeter observations [*Schlax and Chelton*, 1994]. The two peaks at 115 and 165 days are just resolvable from one another using all

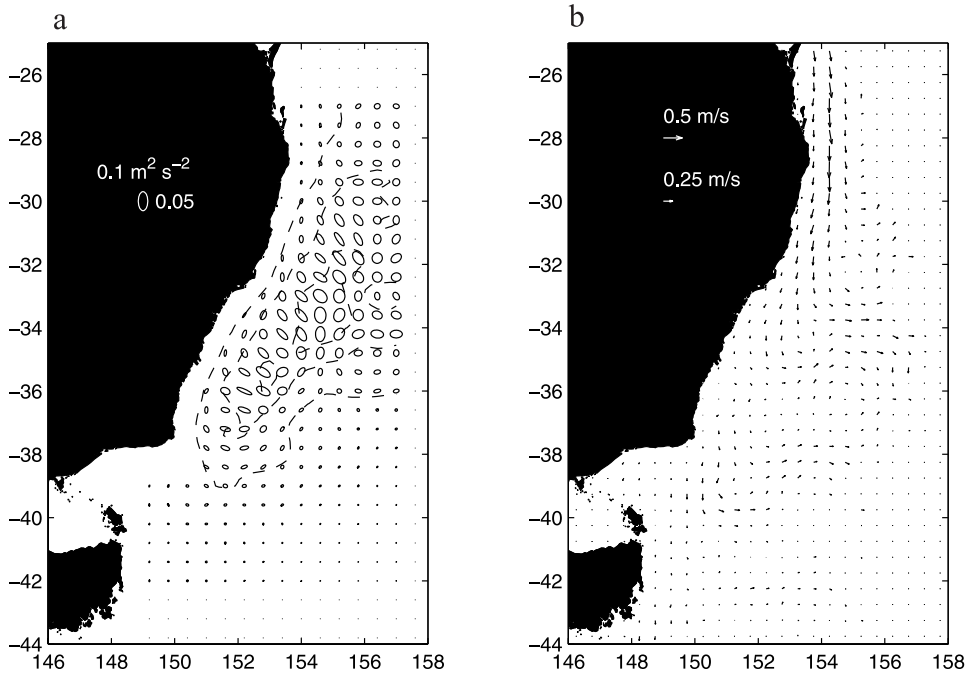

Figure 5. (a) Variance ellipses from the geostrophic velocities with contours of eddy kinetic energy at 0.03, 0.06, and 0.09 $m^2\ s^{-2}$. (b) Mean flow derived from 6 years of MCC velocities showing the highest eddy kinetic energy where the mean flow turns from the coast.

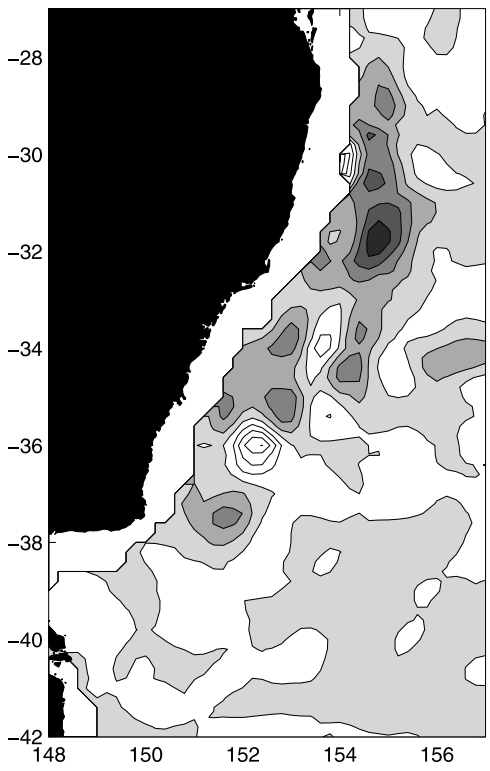

Figure 6. Sum of the barotropic conversion terms, shaded where negative. Contour intervals are $5 \times 10^{-9}\ m^2\ s^{-3}$. Negative values indicate an energy transfer from the mean flow to the eddies.

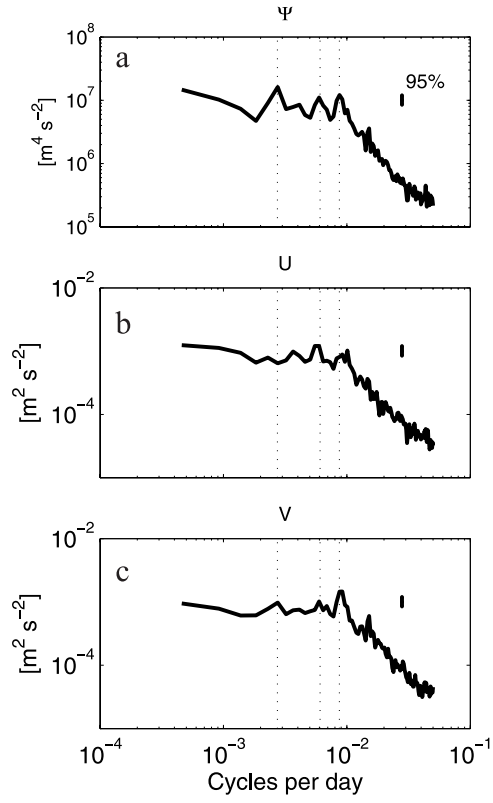

Figure 7. Regional spectra of (a) stream function, (b) zonal velocity, and (c) meridional velocity. Dotted lines are drawn through the peaks in the stream function spectrum to mark annual, 165 day, and 115 day periods.

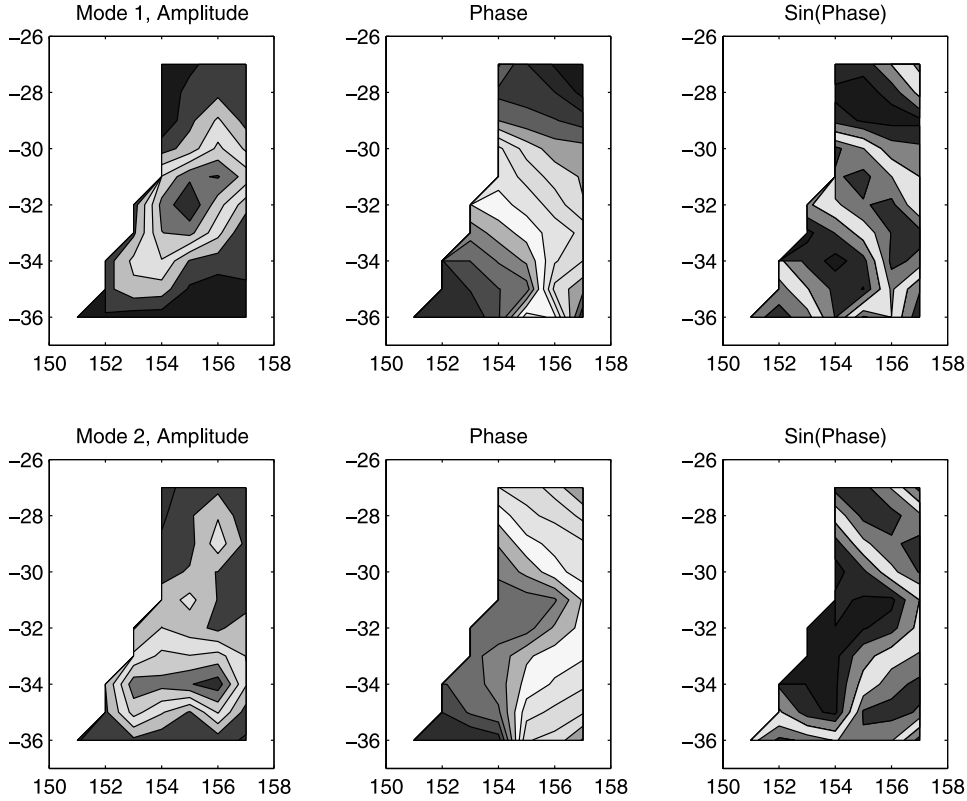

Figure 8. Spatial amplitude and phase of the first two frequency-domain empirical orthogonal functions (EOFs) of the mesoscale band. The phase has been "unwrapped" to show the phase progression from low (blue) to high (red) in $\pi/4$ intervals. The sine of the phase is also plotted to show crests and troughs. The modes explain 40% and 20% of the variance in the band. See color version of this figure at back of this issue.

the measurements in the region. In order to follow energy in space and time the two frequencies will be treated together as one mesoscale band.

[23] The wavelengths of the oscillations are between 500 and 800 kilometers and are too large compared to the size of the domain to be well resolved in a frequency−wave number diagram. Instead we used frequency domain EOFs computed over the entire region to describe the spatial patterns of the mesoscale variability. Much of the southern portion of the domain did not contribute to the first two modes and a repeat analysis on points north of 37°S produced nearly identical results. For this northern region, the mesoscale frequencies comprised about 50% of the total variance. The first two modes describe 40% and 20% of the variance in the mesoscale band.

[24] The first mode captures southwestward propagation with a wavelength of about 600 km or about one and a half wavelengths in the region (Figure 8). The amplitude of the second mode is concentrated near the separation region where it describes primarily westward, or onshore, propagation. The amplitude in the north is much smaller and phase increases in the southwestward direction, as with mode 1. The spatial phases of the two modes are similar south of 33°S and out phase north of this latitude.

[25] The temporal phase and amplitude of the two modes describe the evolution of the two modes over the 6 years (Figure 9). When the temporal phases of the two modes are out of phase with one another, southwestward propagation in the northern part of the domain is more prominent. When the temporal phases of the two modes are in phase, westward motion in the southern part of the region is emphasized.

[26] The amplitude of mode 1 is larger in the first 3 years than in the last three. For much of 1994 and 1995 the two modes are also out of phase describing strong southwestward propagation in the northern part of the domain. Mode 2 is comparable to mode 1 for the last 3 years. During 1996 and 1997 the modes are also nearly in phase, describing the intensification of westward fluctuations in the separation region during these years.

[27] Variance in the mesoscale band can be viewed in both time and space using the wavelet transform (Figure 10) along lines parallel to the Australian coast (Figure 1, dashed line). The region of highest eddy activity appears to move south from 1993, before decreasing to background levels in 1998. The most active region is situated between 30°S and 32°S during 1993 but by the end of 1996 this region has very little variance while a region between 33°S and 35°S is most active. Another location of eddy activity appears in the north between 1995 and 1997. The yearly variance of the stream function in the region decreases by 20% over the 6 years.

3.2. Relationship to Variability in the Subtropical Gyre

[28] The EOFs show anomalies in sea surface height propagating southwestward from the northeastern edge of the domain, suggesting a possible connection with sources

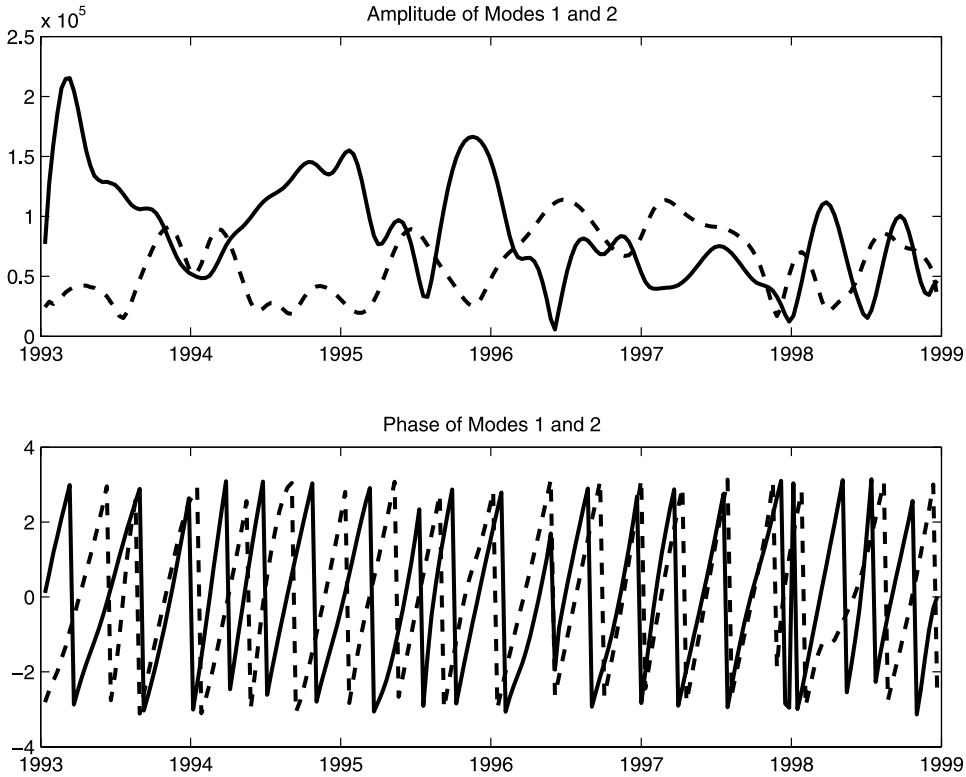

Figure 9. Temporal amplitude and phase of mode 1 (solid lines) and mode 2 (dashed lines) frequency-domain EOFs.

of mesoscale activity to the northeast. Sea surface height variance is elevated in a region of the western Pacific between 20°S and 30°S (Figure 11a) with a band of frequencies and wave numbers similar to the mesoscale band in the EAC.

[29] A connection to the East Australian Current looks most likely at 27°S where a narrow, zonal band of variability extends between 160°E and 165°E over the Lord Howe Rise. Animations show westward movement of height anomalies but no obvious connection between the variability crossing the Lord Howe Rise and the variability in the East Australian Current. Sea surface height shows what appears to be a general westward propagation of highs and lows (Figure 11b). When the mesoscale frequencies are isolated using wavelets (Figure 11c), there is no sign of any coherent signal traveling across the gyre at this latitude or at other latitudes.

[30] A more detailed look at the sea surface height along a path following the region of elevated variance from 170°E westward across the Lord Howe Rise and into the EAC proper (connecting with the 150km along-shore diagram at 31°S) (Figure 12a) shows highs and lows crossing the Lord Howe Rise at times line up with those in the current and at other times do not (Figure 12b). Variance of the mesoscale frequencies (Figure 12c) in the region just west of the Lord Howe Rise (near 2000 km along the path) reaches significant

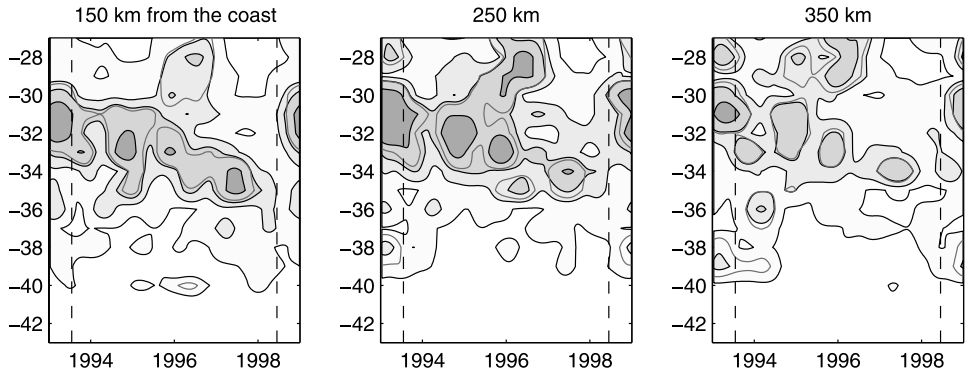

Figure 10. Energy in wavelet transform of the mesoscale frequency band along lines parallel to the Australian coast. Contours are at 1, 2, 5, and 10 times the variance of all the data in the region. Red contours enclose regions where the variance is significantly different from a red noise spectrum at the 95% level at that location. See color version of this figure at back of this issue.

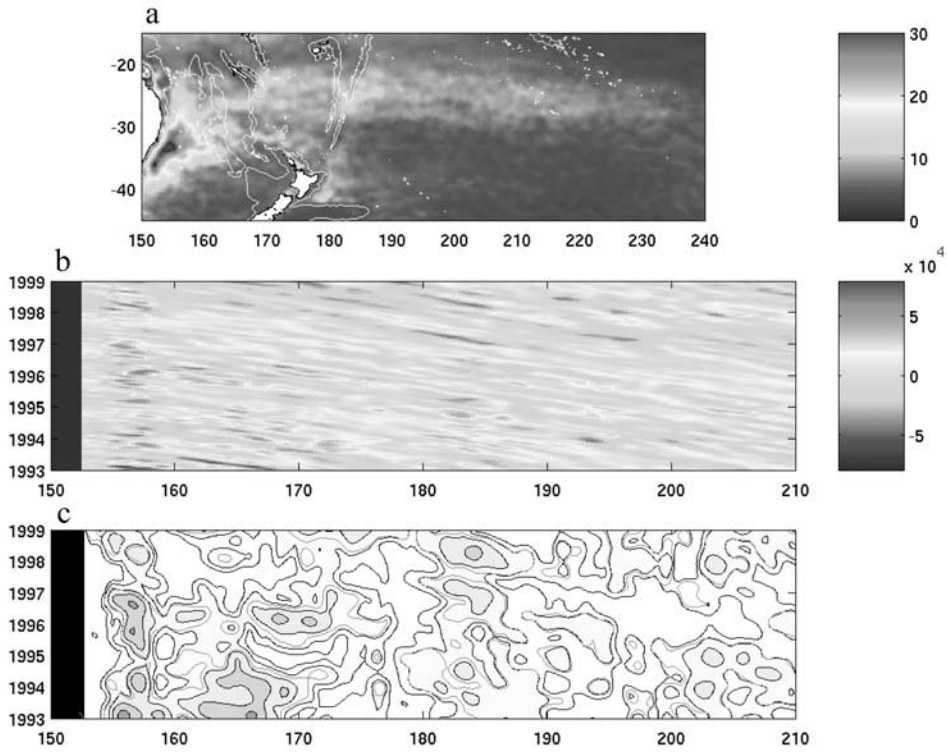

Figure 11. (a) An elevated region of sea surface height anomaly (standard deviation in centimeters) to the northwest of the East Australian Current. (b) Sea surface height across the South Pacific basin at 27°S showing propagating features. (c) Variance in the mesoscale band (plotted in the same manner as the previous figures) showing no coherent signals crossing the gyre at this latitude. See color version of this figure at back of this issue.

levels only during 1993, when it elevated simultaneously both in the EAC proper and east of the Lord Howe Rise, and in 1996 at the end of several years of activity in the north of the EAC. Apart from these two instances, variance west of the rise is very low. Variability in the EAC persists for years without evidence of activity crossing the Lord Howe Rise and, at the end of the time series, appears to renew with no sign of activity to the northeast beforehand.

4. Discussion

[31] Much of the mesoscale variability in the EAC can be described by two EOFs. The first describes southwestward propagation over much of the region and the second primarily westward propagation between 32°S and 35°S. The directions of propagation are consistent with previous observations [*Cresswell and Legeckis*, 1986; *Boland*, 1979; *Nilsson and Cresswell*, 1981]. The simple patterns suggest the reflection of a Rossby wave might be an initial kinematic description of the variability in the current. However, for the range of realistic parameters (wavelengths, frequencies, coastline angles, baroclinic/barotropic wave speeds) the phase and energy directions of incident and reflecting waves vary widely. Given that the real situation is far more complex, with a strong mean flow and interaction between incident and reflected waves, the plane wave example serves only to illustrate that a wide range of responses is possible in even a simple case.

[32] A more realistic case is considered by *Pedlosky* [1993]. Motivated in part by the EAC, he solves for the most unstable mode of a broad baroclinic current along an inclined coast. The wave reflects off the coast and creates a barotropic current within a deformation radius of the coast and flowing in a direction opposing the mean flow. This mechanism might be responsible for some of the variability: we often see thin wedges of cold water near the coast in thermal imagery and these have been shown to coincide with strong barotropic northward flows during the eddy shedding process [*Mata et al.*, 2000]. However, north of 32°S the amplitude of the first EOF (Figure 8) and the region of high eddy variance (Figure 5a) extend well east of the main current in both the climatological dynamic height (Figure 1) and the mean MCC velocities (Figure 5b). The displacement of the variability in this region from the mean kinetic energy suggests it is not created by local baroclinic instability. Indeed, *Stammer* [1997] suggests barotropic fluctuations might play a larger role in the variability. The barotropic conversion terms (Figure 6) are negative in much of the region indicating energy from the mean flow may drive the eddies. The highest values of the conversion are in the separation region corresponding to the highest magnitudes of the eddy kinetic energy.

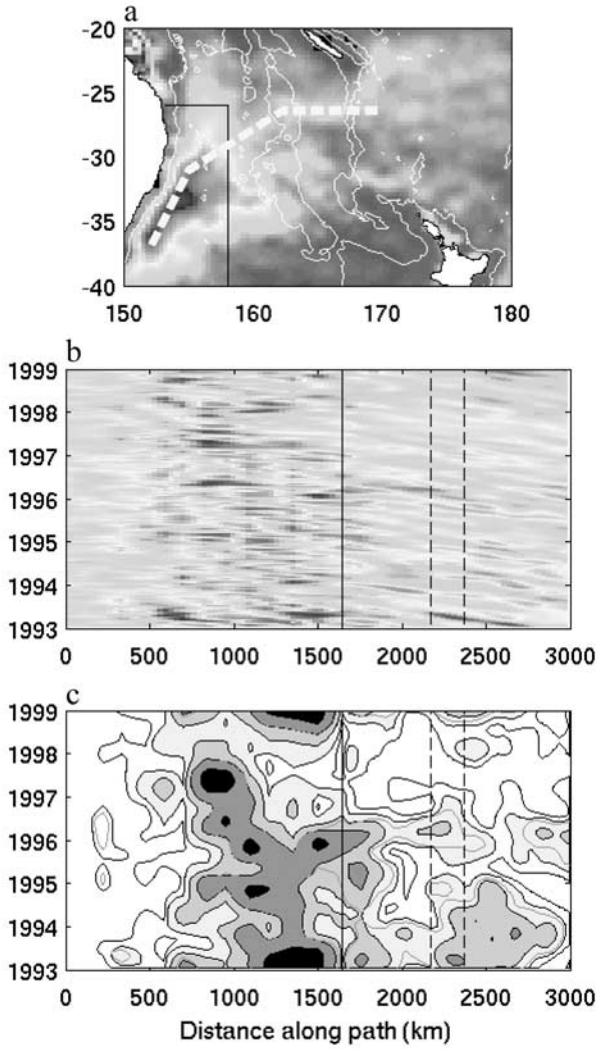

Figure 12. (a) Region covered by the stream function derived in this study, indicated in black. The yellow dashed line indicates a path for variations in the gyre to cross the Lord Howe Rise and into the East Australian Current (EAC). White lines show the 1500 m isobath. (b) Stream function along the path, using the AVISO mapped product (right of the solid line) and the optimal interpolation described in the text (left of the solid line), showing features propagating along the path (scale is the same as in Figure 12a). The position of the 1500 m isobaths marking the Lord Howe Rise are shown by dashed lines. (c) Variance in the mesoscale band (contoured as in Figure 10) showing little connection between the EAC and the Lord Howe Rise. See color version of this figure at back of this issue.

[33] We investigated whether variations in the current are instead directly forced by a band of mesoscale activity to the northeast of the EAC. There is little sign of mesoscale energy traveling coherently from the region of elevated activity into the current either along a constant latitude (Figure 11) or following the path of highest variance into the current (Figure 12). For most of the time series the region immediately west of the Lord Howe Rise has very low variability. There is the appearance of a connection across the Lord Howe Rise during 1993, but to drive the variability in the EAC the connection would have to trigger oscillations in the current for many years afterward. A similar connection does not appear to occur in the years leading up to the renewal of activity in the EAC at the end of 1998.

[34] Within the EAC the region of highest mesoscale variance moves slowly southward from about 31°S in 1993 to near 34°S in 1998 (Figure 10). The change in location of the activity is also evident when the second EOF, whose maximum amplitude is farther south than the first EOF, becomes a larger contributor to the total signal. The second EOF also describes more westward propagation, reinforced by the first EOF when the two come into phase during the last 3 years of the time series. The transition from southwestward to westward propagation is also accompanied by a general decline of energy in the region over the 6 years, with 1998 being the least energetic. There is no obvious sign of a change in inflow transport driving the change in variability: the MCC surface currents show no trend in the strength of the main inflow north of 30°S over the 6 years.

[35] During 1995 and 1996 the wavelets also show an area of elevated variance north of the separation region and well east of the main current (Figure 10) that does not appear to travel southward. It may have been carried north by the return flow or possibly propagated north from the separation region where the barotropic conversion terms suggest the mean flow is losing energy to the eddies (Figure 6). If the EOFs are picking out phase velocities of Rossby wave motions, southward phase velocity would correspond to a northward energy flow, consistent with the variance in the wavelet analysis leaving the separation region and moving to the northeast.

[36] The observed directions of propagation have been used in other studies to infer a mechanism forcing variability in the current. *Cresswell and Legeckis* [1986] suggest the arrival from the north of "geopotential ridges" is influential in the variability while *Nilsson and Cresswell* [1981] suggest a wave along the Tasman Front propagates westward to the separation region, reflects off the coast, and pinches off eddies. We have observed propagation in both directions and a change from one type of behavior to another. If southward propagation in the EOFs corresponds to a Rossby wave phase velocity it should indicate a northward flow of energy. Features that appear to arrive from the north could actually be originating in the separation region to the south. While we have not investigated the role of the Tasman Front, we do note that westward phase propagation is a feature of all Rossby waves, whether they carry energy eastward or westward, and does not by itself indicate the arrival of signals from the west. The fate of the variability immediately west of our study region, where the eastward flowing Tasman Front meets the Lord Howe Rise, certainly deserves further investigation as to whether it provides a feedback for variability in the current.

[37] Previous studies of the EAC have assumed remote forcing drives the variability in the current. In this study we find no evidence for a consistent source at mesoscale frequencies forcing the EAC from the gyre to the northeast. We suggest instead that the analyses in this study are consistent with the EAC generating its own variability

between 32°S and 35°S where the strong mean current encounters the changing coastline and separates from the coast.

5. Summary

[38] An analysis of 6 years of surface currents in the EAC shows strong mesoscale variability concentrated at two frequencies with periods between 90 and 180 days. These frequencies propagate southwestward over much of the region with more westward propagation in the region where the main current separates from the coast. We were able to document a change in the nature of the mesoscale over the course of the 6 years: energy in the current moves southward and diminishes and the propagation becomes more westward.

[39] The strongest variability in the EAC region is associated with the separation region and an area extending to the northeast. The variability to the northeast does not coincide with the strong current along the coast suggesting it does not arise due to local baroclinic instability. No evidence can be found for consistent forcing at the mesoscale frequencies from a region of elevated activity in the gyre to the northeast. Rather than a remote signal forcing the current, we suggest that the analyses of propagation and energy are consistent with variability generated in the separation region by the current itself.

[40] **Acknowledgments.** This work was supported by NASA's Physical Oceanography Program as part of the Jason-1 Science Working Team. This support is gratefully acknowledged. M.B. also received support from the NIWA Visiting Scientist Programme. We thank K. Ridgway and M. Mata for early discussions and B. Bhaskaran for helpful comments on EOFs. Comments from two anonymous reviewers improved the manuscript.

References

Archiving, Validation, and Interpretation of Satellite Oceanographic Data (AVISO) (1998), *User Handbook for Sea Level Anomalies (SLAs)*, *Rep. AVI-NT-011-312-CN*, ed. 3.1, Toulouse, France.

Barnett, T. P. (1983), Interaction of the monsoon and Pacific trade wind system at interannual time scales. Part I: The equatorial zone, *Mon. Weather Rev.*, *111*, 756–773.

Boland, F. M. (1979), A time series of expendable bathythermograph (XBT) sections across the East Australian Current, *Aust. J. Mar. Freshw. Res.*, *30*, 303–313.

Bowen, M. M., W. J. Emery, J. L. Wilkin, P. C. Tildesley, I. J. Barton, and R. Knewtson (2002), Extracting multiyear surface currents from sequential thermal imagery using the maximum cross-correlation technique, *J. Atmos. Oceanic Technol.*, *19*, 1665–1676.

Brooks, I. H., and P. P. Niiler (1977), Energetics of the Florida Current, *J. Mar. Res.*, *35*, 163–191.

Cresswell, G. R., and R. Legeckis (1986), Eddies off southeastern Australia, *Deep Sea Res., Part A*, *33*, 1527–1562.

Ducet, N., P.-Y. Le Traon, and G. Reverdin (2000), Global high-resolution mapping of ocean circulation from TOPEX/Poseidon and ERS-1 and -2, *J. Geophys. Res.*, *105*, 19,477–19,498.

Emery, W. J., A. C. Thomas, M. J. Collins, W. R. Crawford, and D. L. Mackas (1986), An objective method for computing advective surface velocities from sequential infrared satellite images, *J. Geophys. Res.*, *91*, 12,865–12,878.

Feron, R. C. V. (1995), The Southern Ocean western boundary currents: Comparison of fine resolution Antarctic model results with Geosat altimeter data, *J. Geophys. Res.*, *100*, 4959–4975.

Godfrey, J. S., G. R. Cresswell, T. J. Golding, and A. F. Pearce (1980), The separation of the East Australian Current, *J. Phys. Oceanogr.*, *10*, 430–440.

Kelly, K. A., and P. T. Strub (1992), Comparison of velocity estimates from advanced very high resolution radiometer in the coastal transition zone, *J. Geophys. Res.*, *97*, 9653–9668.

Le Traon, P. Y., and F. Hernandez (1992), Mapping the oceanic mesoscale circulation: Validation of satellite altimetry using surface drifters, *J. Atmos. Oceanic Technol.*, *9*, 687–698.

Marchesiello, P., and J. H. Middleton (2000), Modeling the East Australian Current in the western Tasman Sea, *J. Phys. Oceanogr.*, *30*, 2956–2971.

Mata, M. M., M. Tomczak, S. Wijffels, and J. A. Church (2000), East Australian Current volume transports at 30°S: Estimates from the World Ocean Circulation Experiment hydrographic sections PR11/P6 and the PCM3 current meter array, *J. Geophys. Res.*, *105*, 28,509–28,526.

Meyers, S. D., B. G. Kelly, and J. J. O'Brian (1993), An introduction to wavelet analysis in oceanography and meteorology: With application to the dispersion of Yanai waves, *Mon. Weather Rev.*, *121*, 2858–2866.

Nilsson, C. S., and G. R. Cresswell (1981), The formation and evolution of East Australian Current warm-core eddies, *Prog. Oceanogr.*, *9*, 133–183.

Pedlosky, J. (1993), The reflection of unstable baroclinic waves and the production of mean coastal currents, *J. Phys. Oceanogr.*, *23*, 2130–2135.

Qiu, B. (1995), Variability and energetics of the Kuroshio extension and its recirculation gyre from the first two-year TOPEX data, *J. Phys. Oceanogr.*, *25*, 1827–1842.

Qiu, B., and S. Chen (2004), Seasonal modulations in the eddy field of the South Pacific, *J. Phys. Oceanogr.*, *34*, 1515–1527.

Ridgway, K. R., and J. R. Dunn (2003), Mesoscale structure of the mean East Australian Current system and its relationship with topography, *Prog. Oceanogr.*, *56*, 189–222.

Schlax, M. G., and D. B. Chelton (1994), Aliased tidal errors in TOPEX/Poseidon sea surface height data, *J. Geophys. Res.*, *99*, 24,761–24,775.

Schmetz, J., and M. Nuret (1987), Automatic tracking of high-level clouds in Meteosat infrared images with a radiance windowing technique, *Eur. Space Agency J.*, *11*, 275–286.

Schouten, M. W., W. P. M. de Ruijter, and P. J. van Leeuwen (2002), Upstream control of Agulhas ring shedding, *J. Geophys. Res.*, *107*(C8), 3109, doi:10.1029/2001JC000804.

Stammer, D. (1997), Global characteristics of ocean variability estimated from regional TOPEX/Poseidon altimeter measurements, *J. Phys. Oceanogr.*, *27*, 1743–1769.

Tilburg, C. E., H. E. Hurlburt, J. J. O'Brien, and J. F. Shriver (2001), The dynamics of the East Australian Current system: The Tasman Front, the East Auckland Current, and the East Cape Current, *J. Phys. Oceanogr.*, *31*, 2917–2943.

Torrence, C., and G. P. Compo (1998), A practical guide to wavelet analysis, *Bull. Am. Meteorol. Soc.*, *79*, 61–78.

Trenberth, K. E., W. G. Large, and J. G. Olson (1990), The mean annual cycle in global ocean wind stress, *J. Phys. Oceanogr.*, *20*, 1742–1760.

Walker, A. E., and J. L. Wilkin (1998), Optimal averaging of NOAA/NASA Pathfinder satellite sea surface temperature data, *J. Geophys. Res.*, *103*, 12,869–12,883.

Wilkin, J. L., and R. A. Morrow (1994), Eddy kinetic energy and momentum flux in the Southern Ocean: Comparison of a global eddy-resolving model with altimeter, drifter, and current-meter data, *J. Geophys. Res.*, *99*, 7903–7916.

Wilkin, J. L., M. M. Bowen, and W. J. Emery (2002), Mapping mesoscale currents by optimal interpolation of satellite radiometer and altimeter data, *Ocean Dyn.*, *53*, 95–103.

Zhang, D., T. N. Lee, W. E. Johns, C.-T. Liu, and R. Zantopp (2001), The Kuroshio east of Taiwan: Modes of variability and relationship to interior ocean mesoscale eddies, *J. Phys. Oceanogr.*, *31*, 1054–1074.

M. Bowen, National Institute of Water and Atmospheric Research, 301 Evans Bay Parade, Wellington, New Zealand. (m.bowen@niwa.cri.nz)

W. J. Emery, Colorado Center for Astrodynamics Research, University of Colorado, Boulder, CO 80309, USA. (emery@frodo.colorado.edu)

J. L. Wilkin, Institute of Marine and Coastal Sciences, Rutgers University, 71 Dudley Road, New Brunswick, NJ 08901-8521, USA. (wilkin@imcs.rutgers.edu)

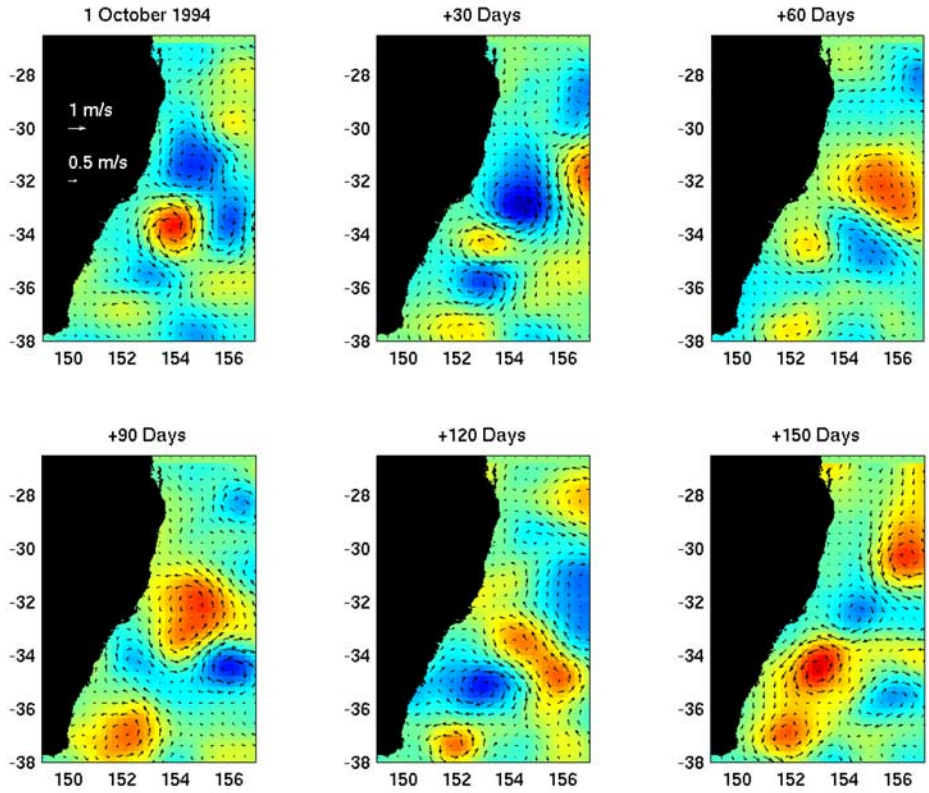

Figure 4. Snapshots of stream function anomaly and associated geostrophic current anomaly over a 150 day period showing alternating cyclones and anticyclones.

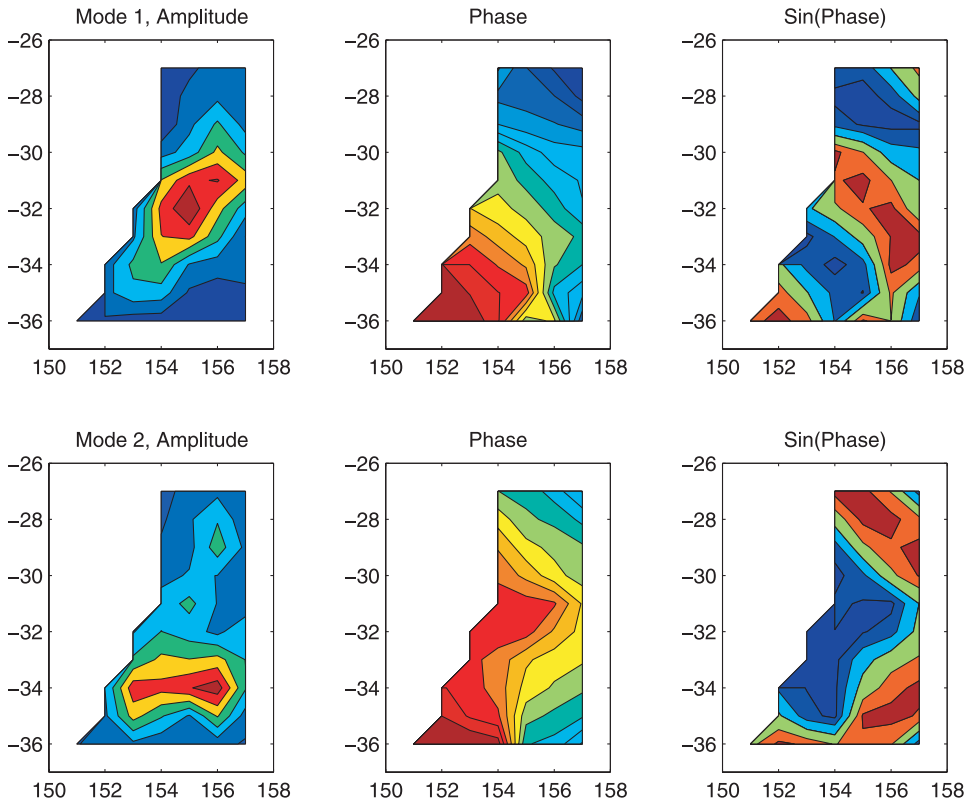

Figure 8. Spatial amplitude and phase of the first two frequency-domain empirical orthogonal functions (EOFs) of the mesoscale band. The phase has been "unwrapped" to show the phase progression from low (blue) to high (red) in $\pi/4$ intervals. The sine of the phase is also plotted to show crests and troughs. The modes explain 40% and 20% of the variance in the band.

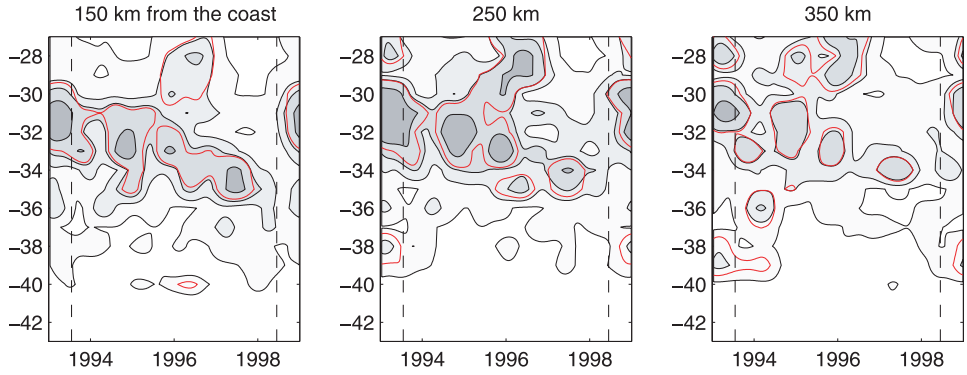

Figure 10. Energy in wavelet transform of the mesoscale frequency band along lines parallel to the Australian coast. Contours are at 1, 2, 5, and 10 times the variance of all the data in the region. Red contours enclose regions where the variance is significantly different from a red noise spectrum at the 95% level at that location.

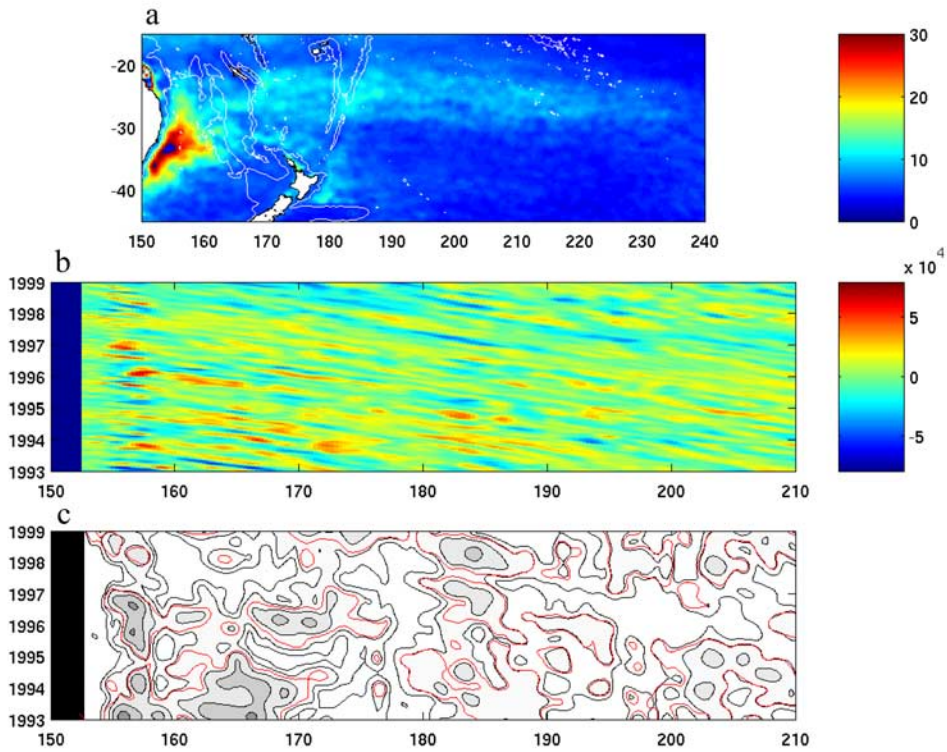

Figure 11. (a) An elevated region of sea surface height anomaly (standard deviation in centimeters) to the northwest of the East Australian Current. (b) Sea surface height across the South Pacific basin at 27°S showing propagating features. (c) Variance in the mesoscale band (plotted in the same manner as the previous figures) showing no coherent signals crossing the gyre at this latitude.

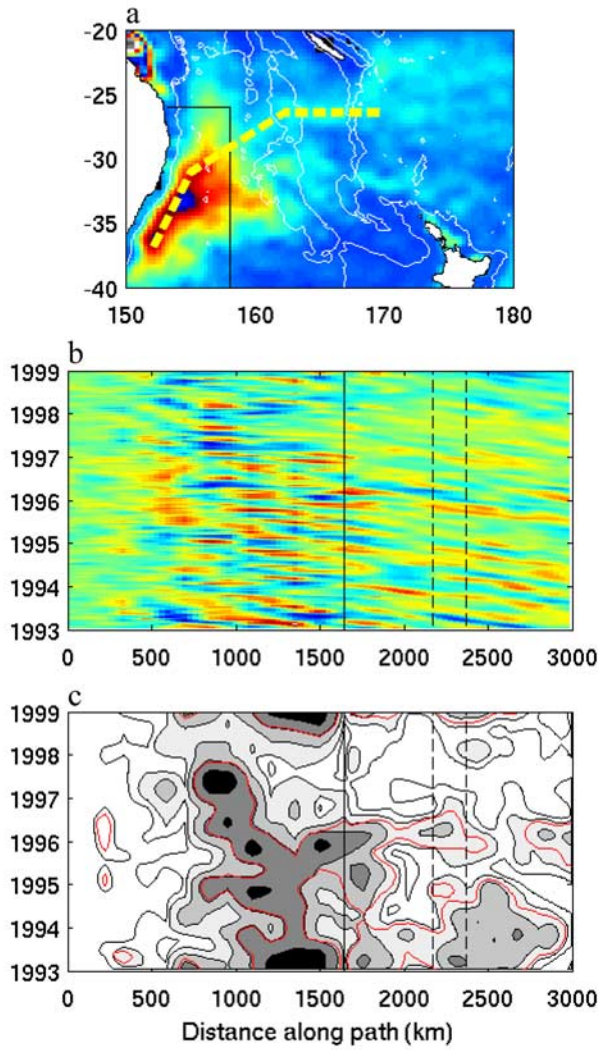

Figure 12. (a) Region covered by the stream function derived in this study, indicated in black. The yellow dashed line indicates a path for variations in the gyre to cross the Lord Howe Rise and into the East Australian Current (EAC). White lines show the 1500 m isobath. (b) Stream function along the path, using the AVISO mapped product (right of the solid line) and the optimal interpolation described in the text (left of the solid line), showing features propagating along the path (scale is the same as in Figure 12a). The position of the 1500 m isobaths marking the Lord Howe Rise are shown by dashed lines. (c) Variance in the mesoscale band (contoured as in Figures 12a and 12b) showing little connection between the EAC and the Lord Howe Rise.